



HAL
open science

Global three-dimensional draping of magnetic field lines in Earth's magnetosheath from in-situ spacecraft measurements

Bayane Michotte de Welle, Nicolas Aunai, Gautier Nguyen, Benoit Lavraud,
Vincent Génot, Alexis Jeandet, Roch Smets

► To cite this version:

Bayane Michotte de Welle, Nicolas Aunai, Gautier Nguyen, Benoit Lavraud, Vincent Génot, et al..
Global three-dimensional draping of magnetic field lines in Earth's magnetosheath from in-situ space-
craft measurements. 2022. hal-03841364v1

HAL Id: hal-03841364

<https://cnrs.hal.science/hal-03841364v1>

Preprint submitted on 7 Nov 2022 (v1), last revised 14 Nov 2023 (v2)

HAL is a multi-disciplinary open access archive for the deposit and dissemination of scientific research documents, whether they are published or not. The documents may come from teaching and research institutions in France or abroad, or from public or private research centers.

L'archive ouverte pluridisciplinaire **HAL**, est destinée au dépôt et à la diffusion de documents scientifiques de niveau recherche, publiés ou non, émanant des établissements d'enseignement et de recherche français ou étrangers, des laboratoires publics ou privés.

1 **Global three-dimensional draping of magnetic field**
2 **lines in Earth's magnetosheath from in-situ spacecraft**
3 **measurements**

4 **B. Michotte de Welle¹, N. Aunai¹, G. Nguyen², B. Lavraud³, V. Génot⁴, A.**
5 **Jeandet¹, R. Smets¹**

6 ¹CNRS, Ecole polytechnique, Sorbonne Université, Université Paris Sud, Observatoire de Paris, Institut
7 Polytechnique de Paris, Université Paris-Saclay, PSL Research University, Laboratoire de Physique des
8 Plasmas, Palaiseau, France

9 ²Direction Générale de l'Armement, France

10 ³Laboratoire d'Astrophysique de Bordeaux, Université Bordeaux, CNRS, Pessac, France

11 ⁴Institut de Recherche en Astrophysique et Planétologie, CNRS, Université de Toulouse, CNES, Toulouse,
12 France

13 **Key Points:**

- 14 • Global 3D reconstruction of the magnetic field draping around the Earth magne-
15 tosphere purely from in situ observations
16 • Draping pattern is shown as a function of the interplanetary magnetic field cone
17 angle
18 • The role of the magnetosheath flow to which the magnetic field is frozen is em-
19 phasized by a comparison to a vacuum magnetostatic draping

Corresponding author: B. Michotte de Welle, bayane.michotte-de-welle@lpp.polytechnique.fr

20 **Abstract**

21 Magnetic field draping occurs when the magnetic field lines frozen in a plasma flow wrap
 22 around a body or plasma environment. The draping of the interplanetary magnetic field
 23 (IMF) around the Earth’s magnetosphere has been confirmed in the early days of space
 24 exploration. However, its global and three-dimensional structure is known from mod-
 25 eling only, mostly numerical. Here, this structure in the dayside of the Earth’s magne-
 26 tosheath is determined as a function of the upstream IMF orientation purely from in-
 27 situ spacecraft observations. We show the draping structure can be organized in three
 28 regimes depending on how radial the upstream IMF is. Quantitative analysis demon-
 29 strates how the draping pattern results from the magnetic field being frozen in the mag-
 30 netosheath flow, deflected around the magnetopause. The role of the flow is emphasized
 31 by a comparison of the draping structure to that predicted to a magnetostatic draping.

32 **1 Introduction**

33 Magnetic field draping is a universal phenomenon in highly conducting magnetized
 34 astrophysical plasmas. It is known to occur around induced (McComas et al., 1986; Bertucci
 35 et al., 2011; Rong et al., 2014; Delva et al., 2017; C. Zhang et al., 2022) and intrinsic plan-
 36 etary magnetospheres ((Fairfield, 1967; Behannon & Fairfield, 1969; Kaymaz et al., 1996)),
 37 comets (Reidler et al., 1986; Koenders et al., 2016), solar ejecta in the IMF (McComas
 38 et al., 1988; Jones et al., 2002; Kaymaz & Siscoe, 2006), the heliosphere in the interstel-
 39 lar field (Opher et al., 2007; Pogorelov et al., 2021), galaxies in the intergalactic field (Pfrommer
 40 & Dursi, 2010). Magnetic field draping is key in understanding how plasma environments
 41 couple with their surroundings. In particular it is of pivotal importance in determining
 42 the location, triggering and efficiency of magnetic reconnection at magnetic boundaries
 43 (Cassak & Fuselier, 2016; Trattner et al., 2021).

44 The closest example of magnetic field draping is found in the Earth’s magnetosheath,
 45 where the IMF drapes around the magnetopause. This region thus constitutes a unique
 46 observatory for in-situ measurements of this ubiquitous plasma process. Predicted theo-
 47 retically from the transport of field lines in gas dynamics models (Spreiter et al., 1966),
 48 the draping effect was first evidenced in the magnetosheath the following couple of years
 49 (Fairfield, 1967; Behannon & Fairfield, 1969) in spacecraft in-situ measurements, although
 50 very few data points were accessible at the time. Increasingly more detailed observations
 51 were subsequently performed (Crooker et al., 1985; Ohtani & kokubun, 1991; Kaymaz
 52 et al., 1992; Kaymaz, 1998; Coleman, 2005; Longmore et al., 2006; Petrinec, 2016), con-
 53 firming the draping of the IMF and comparing the orientation of the magnetic field lo-
 54 cally measured in the magnetosheath, to that predicted by models. These observations
 55 were, however, restricted to coarse angular sectors of the IMF orientations and to par-
 56 ticular orbital planes. Our current understanding of how the magnetic field drapes around
 57 the magnetosphere in a global and three-dimensional manner and as a function of the
 58 IMF orientation thus only comes from analytical ((Kobel & Fluckiger, 1994; Kallio &
 59 Koskinen, 2000; Vandas & Romashets, 2019)) and numerical modeling ((Kaymaz, 1998;
 60 Turc et al., 2014)). Half a century after the first models of the magnetic field draping
 61 in the magnetosheath (Spreiter et al., 1966), there is still so far no consistent equivalent
 62 from a purely observational standpoint. This is the goal of this study.

63 An example of in-situ spacecraft data measured in the near-Earth environment, is
 64 given on Fig. 1a-d. The data shows the signatures typically seen in an outbound tra-
 65 jectory from the magnetosphere to the solar wind, going through the magnetosheath re-
 66 gion. The magnetosphere is characterized by the strongest magnetic field amplitude, low-
 67 est density and most stagnant plasma of all three regions. The solar wind is easily rec-
 68 ognized as a comparatively dense plasma flowing at supersonic speed during the last part
 69 of the time interval. The magnetosheath is the region in between these two, downstream
 70 of the bow shock where the plasma is heated, compressed, and flows around the obsta-

71 cle after having been decelerated to a subsonic speed. In that region, the magnetic field
 72 increases in amplitude and drapes around the magnetopause.

73 Obtaining the global and three-dimensional magnetic field draping pattern as a func-
 74 tion of the IMF orientation, from only in situ data, intrinsically local in space and time,
 75 is actually quite challenging. Firstly, the data is heavily spatially biased by the satellite
 76 orbital planes. Reconstructing a global draping from observations thus imperiously re-
 77 quires having multiple spacecraft on significantly different orbits. Secondly, understand-
 78 ing the dependence of the draping on the IMF orientation requires the constant moni-
 79 toring of the upstream solar wind from yet another spacecraft. And even if such data
 80 is available, estimating the causal IMF orientation for each magnetosheath measurement
 81 may come with possibly substantial errors that call for large statistics for the results to
 82 be relevant. Then, the magnetosheath flow carries many small scale plasma and mag-
 83 netic fluctuations from which the macroscale field can only stand out if using again a large
 84 number of uncorrelated measurements. Unfortunately, the complexity of the time series
 85 makes it difficult to automatize the identification of time intervals during which the space-
 86 craft explores regions of interest. Data selection is often performed manually, hamper-
 87 ing large statistics, consequently adding substantial uncertainties when drawing conclu-
 88 sions. Last but not least is the fact that multivariate time series like that shown in Fig.
 89 1 actually represent slices in an unsteady complex three-dimensional system in which the
 90 instantaneous position of the spacecraft relative to plasma structures is unknown. This
 91 space/time ambiguity substantially complicates the the spatial representation of the drap-
 92 ing pattern, which requires the magnetic field measured at a given time to be positioned
 93 relative to the magnetopause and the bow shock boundaries.

94 Decades of in-situ measurements from a fleet of spacecraft that have been or still
 95 are exploring the near-Earth environment are now accessible. Many of these missions
 96 have been operating at a time when solar wind monitoring was available. In this study,
 97 statistical learning was key to automatically detect all time intervals during which Clus-
 98 ter, Double Star, THEMIS and MMS spacecraft have measured magnetosheath data, as
 99 explained in section 2. This allowed us to gather of 45 million magnetosheath in-situ mea-
 100 surements at 5 second resolution over a period of two decades, offering an excellent spa-
 101 tial coverage of the 3D dayside magnetosheath. The dataset also offers a very good cov-
 102 erage of the distribution of the IMF clock ($\theta_{cl} = \arctan^{-1}(B_y/B_z) \in [-\pi, \pi]$) and cone
 103 ($\theta_{co} = \arctan^{-1}(\sqrt{B_y^2 + B_z^2}/B_x) \in [-\pi/2, \pi/2]$) angles, as visible on figures Figure 1f
 104 and g, where essentially no difference is visible between the distribution of these two an-
 105 gles for the whole OMNI data and the considered subset. Machine learning was also an
 106 asset in positioning each individual magnetosheath measurements relatively to the mag-
 107 netopause and bow shock, by enabling the prediction of these boundaries' position given
 108 upstream solar wind/IMF parameters, as explained in section 2.

109 This work offers a global and detailed three-dimensional statistical representation
 110 of the magnetic field draping around the magnetosphere, as a function of the IMF ori-
 111 entation and from in situ observations only. The statistical representation of the observed
 112 draping will be compared to the one obtained by a magnetostatic model (Kobel & Fluck-
 113 iger, 1994). This comparison is made not because such model can be considered as re-
 114 alistic as, say, the result of a global MHD numerical model. But, assuming the draping
 115 occurs in vacuum, this model offers an interesting contrast we use to emphasize the key
 116 role played by the magnetosheath flow in structuring the draping for various IMF ori-
 117 entations. Moreover, this draping model is broadly used by researchers and has been at
 118 the root of studies of the dynamics of cosmic dust (Juhász & Horányi, 1999), spacecraft
 119 fine debris (Juhász & Horányi, 1997) and many other plasma processes occurring not only
 120 in the Earth's magnetosheath (e.g. (Génot et al., 2011)), but also in that of other plan-
 121 ets such as Mercury (Schmid et al., 2021a, 2021b), Jupiter (Masters, 2017), Saturn (Sulaiman
 122 et al., 2014), Uranus (Masters, 2014) and Neptune (Masters, 2015). It is a key ingredi-
 123 ent in how researchers nowadays predict where reconnection may occur at the magne-

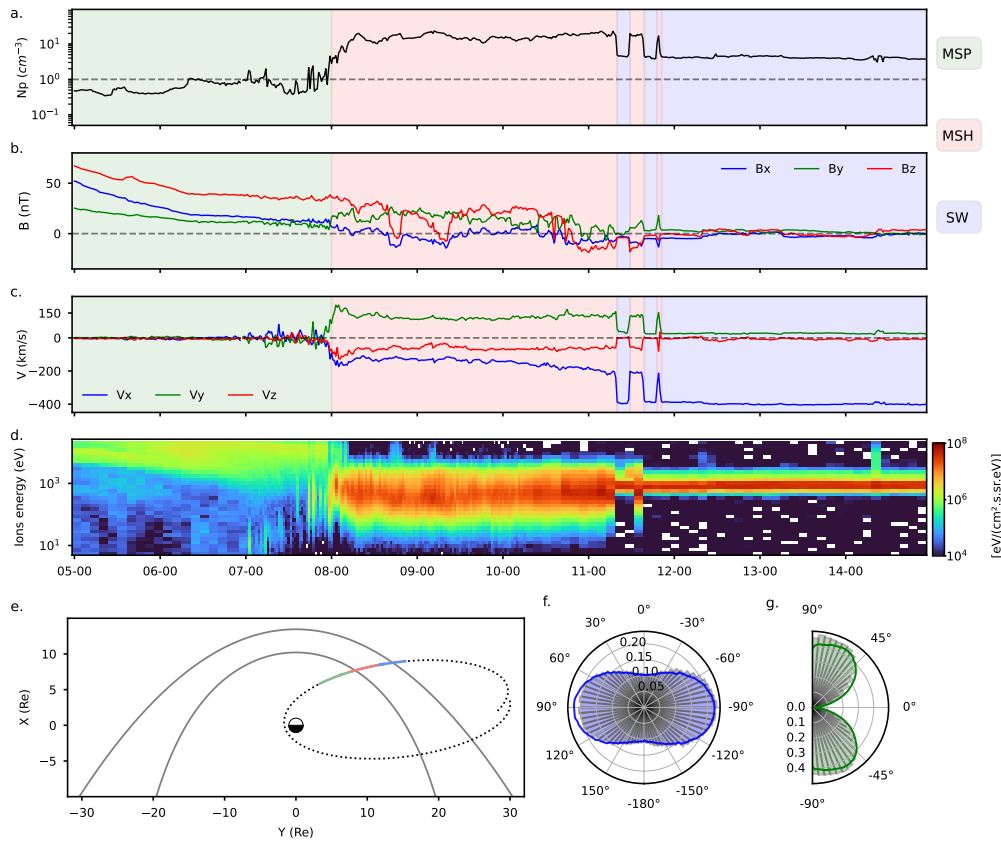


Figure 1. In-situ data and orbit from THEMIS B probe on May 16 2008. Panels a to d show respectively the ion density, the magnetic field components, the velocity components, the omnidirectional energy fluxes of ions. Panel e shows in the orbit of the probe on a 5-day period with the dotted line. The bow shock (Jelínek et al., 2012) and magnetopause (Shue et al., 1998) are represented as solid gray lines. In a-c and e, the green, red, and blue color filling and line colors correspond to the time intervals automatically classified by the machine learning algorithm as magnetosphere, magnetosheath and solar wind respectively. The blue and green histograms in f and g correspond to the polar density distribution of the IMF clock and cone angle, respectively, for all times associated with magnetosheath measurements. The blue and green solid lines represent the same distributions but for the whole twenty-six years of OMNI data.

124 topause for a given upstream IMF orientation (Trattner et al., 2021). Very recently, the
 125 same analytical approach has been undertaken with more realistic boundary geometries
 126 (Vandas & Romashets, 2019) and compared to THEMIS observations (Vandas et al., 2020),
 127 but still without coupling the magnetic field to the flow. We then use the independent
 128 measurements of the ion bulk velocity, together with the magnetic field measurements,
 129 to quantitatively demonstrate that the detailed structure of the observed draping results
 130 from the magnetic field being frozen in the deflected magnetosheath flow.

131 Section 2 describes the data and the methodology used to obtain the results, which
 132 are presented in section 3. Section 4 concludes this paper.

133

2 Method

134

2.1 From local measurement to global representation of the magnetosheath magnetic field : Pipeline overview

135

136

137

138

139

140

141

142

143

144

145

146

147

148

149

150

151

152

153

154

155

156

157

158

159

160

This section provides an overview of the processing pipeline, graphically represented on Fig. 2, designed to obtain a continuous representation of the magnetic field lines in the magnetosheath for a given IMF orientation using only in situ measurements. Details associated with each step of this pipeline are given in following subsections. Data from four spacecraft missions were used (see section 2.2) from 2001 to 2021. The subset of the data corresponding to measurements in the magnetosheath is selected automatically (see section 2.3 for more detailed on the selection method), resulting in about 50 million data points. Studying the draping as a function of the IMF orientation first requires to pair each measurement with the properties of its causal IMF and solar wind. The pairing method is detailed in section 2.4. Measurements for which the solar wind/IMF conditions are not available are eliminated. Due to the finite number of measurements, the draping is reconstructed from the subset of points associated with an IMF orientation within a finite interval, as narrow as possible for accuracy, and large enough for statistical relevance. The selected points are found in between the closest magnetopause and the farthest bow shock for the solar wind and IMF condition subset. As is, these points do not give a fair representation of the spatial structure of the draping because two points close spatially may be at different distance from the magnetopause and bow shock for their respective solar wind and IMF conditions. It is thus necessary to re-position each data point relatively to the same shock and magnetopause. The relative position of each measurement is obtained from a nonparametric regression (see section 2.5) of the radial position of the boundaries as a function of solar wind/IMF conditions. At this point, around 45 million magnetosheath measurements remain, paired with IMF conditions and positioned between the same pair of bow shock and magnetopause models (Jelínek et al., 2012; Shue et al., 1998). Data from in situ measurements do not homogeneously sample the magnetosheath volume for any specific IMF cone and clock angle.

161

162

163

164

165

166

167

168

169

170

171

172

173

174

175

176

177

Obtaining the global and 3D draping pattern with enough statistics thus requires to further assume the pattern is invariant when rotated by the IMF clock angle. In other words, two measurements at different positions in the magnetosheath associated with close enough IMF cone angles are assumed to sample the same continuous draping pattern if rotated by the IMF clock angle. This rotational invariance of the draping pattern is exact for the magnetostatic model and expected to be a good approximation for the draping in reality since processes depending on the IMF clock angle such as magnetic reconnection would only alter the draping in the very close proximity of the magnetopause. Each measurement therefore has its position moved into the so-called Solar Wind Interplanetary (SWI) coordinate system (H. Zhang et al., 2019) (see section 2.6). The draping can then be obtained by selecting data for which the IMF cone angle only is within a small interval around the desired value. The spatial distribution in the magnetosheath of any physical quantity (here the magnetic field and the bulk velocity) is obtained by computing, at any position, the average of this quantity over the K closest measurements, weighted by their distance to the position (see section 2.7). Finally the continuous 3D magnetic field and flow lines are integrated with the method detailed in section 2.8.

178

2.2 Satellites and instrumentation

179

180

181

The in-situ data are provided by the instruments of the four missions shown in Table 1. The data are resampled to a 5s resolution, on which a 3 points median filter is applied to remove outliers.

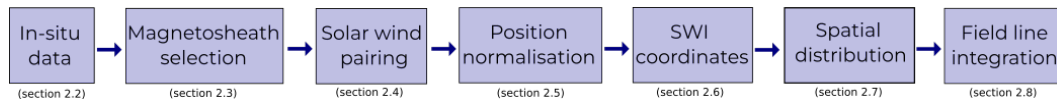


Figure 2. Overview of the data processing pipeline Illustrates the different step of the data processing used to represent the global 3D dayside magnetic field draping pattern from scattered in situ data measurements.

Mission	Probe	Period	Instruments
Cluster	C1	2001-2019	Cluster Ion Spectrometry (CIS) (Rème et al., 2001)
	C3	2001-2009	Fluxgate Magnetometer (FGM) (Balogh et al., 2001)
DoubleStar	TC1	2004-2007	Hot Ion Analyzer (HIA) (Rème et al., 2005) Fluxgate Magnetometer (FGM) (Carr et al., 2005)
Themis	P3, P4, P5	2007-2021	Electrostatic Analyzers (ESA) (McFadden et al., 2008)
	P1, P2	2007-2009	Fluxgate Magnetometer (FGM) (Auster et al., 2008)
Magnetospheric Multiscale	MMS1	2015-2021	Plasma Investigation (FPI) (Pollock et al., 2016) Fluxgate Magnetometer (FGM) (Russell et al., 2016)

Table 1. Source of the in-situ data.

182

2.3 Selection of magnetosheath data

183

184

185

186

187

188

189

190

191

192

193

194

195

196

197

198

199

200

201

202

203

204

205

206

207

208

209

The magnetosheath is a region bounded by the bow shock and the magnetopause, which position and shape are dynamically governed by the solar wind and IMF conditions. Moreover the state of the magnetosheath is strongly related to the conditions in the solar wind and is quite inhomogeneous, from the equator to higher latitude, or from the quasi-parallel side to the quasi-perpendicular (Dimmock et al., 2020). Finding the subset of the whole dataset that corresponds to measurements made in the magnetosheath is thus difficult. A first idea could be to select all measurements made between the position of the magnetopause and the bow shock predicted for upstream solar wind and IMF conditions by analytical models (Dimmock & Nykyri, 2013; H. Zhang et al., 2019). However, the average root mean square error (RMSE) of analytical models of magnetopause is about 1.25 Re (Wang et al., 2013), and is even greater for bow shock models (Merka et al., 2003), resulting in magnetosphere and solar wind measurements polluting the dataset around the boundaries. This also possibly biases the selection of the measurements by modeling assumptions. Magnetosheath measurements can rather be selected based on the properties of the data therein. Using a combination of empirically fixed thresholds characterizing magnetosheath data (Jelinek et al., 2012) is possible but not optimal when considering the entire magnetosheath volume from the subsolar region to the close nightside. Recent work (Nguyen et al., 2022) indeed showed that the magnetosheath data is not linearly separable from that measured in neighboring regions in feature space. Deep learning classification based on convolutional neural networks has recently been shown to reach excellent performances for isolating measurements made in regions such as the magnetosheath (Olshevsky et al., 2021; Breuillard et al., 2020). Similar precision was later obtained with a much faster and simpler Gradient Boosting classifier (Nguyen et al., 2022), using only plasma moments and magnetic field as features. About 50 millions of magnetosheath in-situ measurements are automatically selected. Finally, the aberration on the velocity due to the orbital motion of the Earth has been corrected.

210 **2.4 Solar wind parameters**

211 In this study, each magnetosheath data point is associated to solar wind and IMF
 212 properties (magnetic field, density, temperature, velocity, dynamic pressure, Mach num-
 213 ber, plasma beta) from the OMNI dataset (King & Papitashvili, 2005) measured at a
 214 previous time. The time delay is estimated by using a propagation method adapted from
 215 Safrankova et al. 2002 (Safránková et al., 2002). The distance along the Earth-Sun line
 216 between the nose of the bow shock, at which OMNI data is defined, and the spacecraft
 217 position, is first estimated. The propagation time between these positions is estimated
 218 based on an average solar wind speed. The solar wind velocity is then estimated from
 219 OMNI data as the average over a 5 minutes window centered around the measurement
 220 time to which is subtracted the time delay. A new time delay is estimated based on that
 221 new solar wind speed, and then used as previously to obtain final values of solar wind
 222 and IMF parameters. Further iterations could be made but represent a significant over-
 223 head in the execution of the pipeline as this has to be evaluated for each of the 50 mil-
 224 lions magnetosheath data points. The consistency of the obtained results a posteriori
 225 justifies this is enough but other applications may require a more detailed selection. OMNI
 226 data is used in the boundary regression models (see section 2.5). In addition, each mea-
 227 surement of the magnetic field (resp. the bulk velocity) made in the magnetosheath and
 228 used in this study is normalized by the OMNI magnetic field amplitude (resp. solar wind
 229 velocity).

230 **2.5 Estimating the boundaries position**

231 The measurements must be re-positioned in between a unique pair of magnetopause
 232 and bow shock, which requires the determination of their instantaneous distance rela-
 233 tive to these boundaries. Estimating the relative distance to analytical models of the mag-
 234 netopause and bow shock boundaries is not optimal since it needlessly relies on assump-
 235 tions on their shape and algebraic dependency on solar wind and IMF conditions. These
 236 assumptions lead to substantial errors in the relative radial position estimate, compa-
 237 rable to the thickness of the magnetosheath in the subsolar region (Wang et al., 2013;
 238 Merka et al., 2003). Instead, nonparametric regression of the radial position of the mag-
 239 netopause and bow shock as a function of the angular positions and solar wind/IMF con-
 240 ditions is used. Best performances were reached with the gradient boosting regressor (Pedregosa
 241 et al., 2011) algorithm, trained to predict the radial position of a boundary, given an-
 242 gular positions, IMF orientation and amplitude, solar wind density, bulk velocity vec-
 243 tor, temperature and the Earth dipole tilt angle. The training set was taken as a sub-
 244 set of the 33563 magnetopause and 19361 bow shock single crossings, defined on 10 min-
 245 utes windows identified using the method described in (Nguyen et al., 2022). Crossings
 246 falling in the same solid angle of 7.5° during the same 30 minute intervals were collec-
 247 tively put either in the training set or the test set, to ensure their statistical indepen-
 248 dence. Cross-validation has been performed with a 90/10 split between those two sets
 249 and a Root Mean Square Error (RMSE) of 0.78 ± 0.03 Re for the magnetopause model
 250 and of 0.96 ± 0.06 Re for the bow shock model have been obtained.

251 **2.6 Solar Wind Interplanetary magnetic field coordinate system**

252 The solar wind interplanetary (SWI) magnetic field coordinate system (H. Zhang
 253 et al., 2019) is used in this work. This system depends on the IMF orientation and ve-
 254 locity of the solar wind. The X_{swi} axis is colinear to the solar wind velocity vector and
 255 points towards the sun. The Y_{swi} is define along the magnetic field in the YZ plane. There-
 256 fore the position of each point is rotated so that its IMF component B_{yimf} is positive,
 257 i.e an IMF clock angle of 90° . The magnetic field is furthermore transformed to have B_{ximf}
 258 positive (\mathbf{B} to $-\mathbf{B}$ and \mathbf{B}_{imf} to $-\mathbf{B}_{imf}$ if $B_{ximf} < 0$) so that draping pattern depends
 259 only on the absolute value of the IMF cone angle. Thus, the magnetic field vector ex-
 260 pressed in the SWI coordinate system only has positive components along the X_{swi} and

261 Y_{swi} axis. The rotation of each measurement into the SWI coordinate system implicitly
 262 assumes the axisymmetry of the system. The magnetopause has been shown to develop
 263 non-axisymmetries depending on the IMF clock angle (Nguyen et al., 2022). The differ-
 264 ences visible in the equatorial and meridional flaring, however, are small if considering
 265 only the dayside magnetopause as we do and probably of the order of the errors made
 266 in determining the position of the models in the first place.

267 **2.7 From discrete scattered samples to continuous field maps**

268 This section explains how to produce a continuous spatial representation of a field
 269 from a discrete scattered set of measurements. Space is meshed with regular spacing (resp.
 270 angular spacing) for XY views (resp. YZ views). The field at each mesh node is set to
 271 the prediction of the k-Nearest-Neighbor algorithm, i.e. a weighted average of field's val-
 272 ues over the K nearest measurements to that node (KNeighborsRegressor) (Pedregosa
 273 et al., 2011; Kramer, 2013). The weights are given by the inverse of the distance from
 274 the node where the value is predicted to the i_{th} measurement position $1/d = 1/|r_{node} -$
 275 $r_i|$. Each magnetic field time measurement in the magnetosheath used to train the kNN
 276 is normalized by the IMF magnitude it is associated with in the OMNI data. The po-
 277 sitions used to find the K nearest neighbor measurements are the normalized SWI co-
 278 ordinates obtained in previous steps of the pipeline. The following analysis is made on
 279 subsets of the data for which the IMF cone angle is within a small interval around a
 280 desired value. As visible on Fig. 1, the distribution of the IMF cone angle is non uni-
 281 form, and in particular very small IMF cone angles represent less than 3% of the total
 282 dataset. To keep a similar locality for each map (at the expense of a larger statistical
 283 noise), we thereby use a value of $K = 7500$ for hereafter denoted "low IMF cone an-
 284 gle regime" subsets, while other subsets used $K = 10^4$. Values of K are chosen so that
 285 the median distance of these K nearest points is on average about 0.5 R_e , providing a
 286 reasonable locality while being relatively smooth.

287 **2.8 From discrete scattered samples to 3D continuous magnetic and flow** 288 **lines**

289 The magnetic field lines have been integrated in 3D with Backward Differentiation
 290 Formula (BDF) method. At each step of the integration, the magnetic field is estimated
 291 locally using the KNeighborRegressor (see sec. 2.7). Any small components locally nor-
 292 mal to the magnetopause resulting from statistical noise or from the renormalization pro-
 293 cess are removed within $0.15R_e$ to the boundary. The same line integration method is
 294 used for both magnetic and flow lines throughout this paper. In the case of the magnetic
 295 field, the field line is prolonged in the solar wind by a straight line inclined with respect
 296 to the X_{swi} axis by an angle corresponding to the average value of the IMF cone angle
 297 for the considered subset. All 45 million magnetosheath velocity measurements are used
 298 to determine the streamlines. Therefore it allows to set K as high 45,000 points in the
 299 KNeighborsRegressor while still maintaining a median distance lower than 0.5 R_e .

300 **2.9 Comparison to a magnetostatic model**

301 In this study the draping obtain from the in-situ measurements is compared to the
 302 one resulting from the widely used magnetostatic model of Kobel and Fluckiger 1994 (Kobel
 303 & Fluckiger, 1994). This model assumes the magnetic field derives from a potential, there
 304 is no plasma in the magnetosheath. The same processing pipeline is used to represent
 305 the modeled draping as for the in-situ data (see section 2.1). That is, the local value of
 306 the represented field still is estimated from the spatial average over the K nearest space-
 307 craft positions, but the averaged values now result from modeled predictions at these K
 308 positions rather than actual measurements. The model is defined by a magnetic poten-
 309 tial valid between parabolic and confocal boundaries. Therefore, the estimated relative

310 position to the boundaries (see section 2.5) is used to re-position each point between the
 311 parabolic and confocal boundaries obtained with Eq. 1 (Romashets & Vandas, 2019) :

$$\sin^2(\theta)R_{mp,bs}^2 + 4(x_{0,1} - x_0/2) \cos(\theta)R_{mp,bs} - 4(x_{0,1} - x_0/2)x_{0,1} = 0 \quad (1)$$

312 With θ the elevation angle in respect of the X axis, x_0 and x_1 corresponding to the
 313 standoff distances of the magnetopause and shock respectively. These standoff distances
 314 depends on the solar wind and IMF conditions and are obtained with the same the non-
 315 parametric regression of the boundaries as previously presented. Finally, all positions
 316 are normalized between the same pair of shock and magnetopause before being trans-
 317 formed into the SWI coordinates system (see section 2.6).

318 **3 Results**

319 **3.1 Large IMF cone angle draping**

320 The first comparison, shown in Fig 3, is made for the subset of the data associated
 321 with an IMF cone angle falling within the range $70^\circ \leq |\theta_{co}| \leq 80^\circ$. At such a large
 322 cone angle, the IMF is almost perpendicular to the Sun-Earth axis, as can be seen in the
 323 two leftmost panels, representing the system in the plane containing the IMF. Note that
 324 although the magnetopause and the bow shock are represented by their cross-section in
 325 the $X_{swi}-Y_{swi}$ plane, the magnetic field lines are the projection on that plane of lines
 326 exploring the three dimensions of space. Although small, the B_x component of the mag-
 327 netic field is sufficient to break the symmetry between the two sides of $Y_{swi} = 0$. The
 328 side where the IMF is most parallel to the shock surface normal vector, the so-called quasi-
 329 parallel side is found where $Y_{swi} > 0$, by convention of the SWI coordinate system adopted
 330 here. Respectively, the so-called quasi-perpendicular side is found for $Y_{swi} < 0$. By con-
 331 vention of the SWI system also, the X_{swi} component of the IMF is taken positive.

332 A quick glance at Fig. 3 reveals that the draping obtained with the magnetostatic
 333 model (upper panels a,b,c) is strikingly similar to the one obtained from in-situ data (lower
 334 panels d,e,f). The leftmost panels show that field lines in the quasi-perpendicular side
 335 exit the magnetosheath through the bow shock on the quasi-parallel side.

336 Consistently, the B_x component, positive in the quasi-perpendicular side, goes through
 337 zero around the subsolar region and becomes negative in the quasi-parallel region. The
 338 amplitude of the B_x values are reasonably similar between the model and the data. The
 339 data values seem a bit lower than those of the model but it is unclear to what extent this
 340 difference is physical, considering the model does not account for the dynamical pile up
 341 on the magnetopause and primarily depends on the distance between the two bound-
 342 aries. The lines that appear to cross the magnetopause actually do not, but rise in the
 343 third dimension, above the $Z_{swi} = 0$ plane to circumvent the magnetopause. This is
 344 better seen from the middle panels which represent the field lines close to the magne-
 345 topause surface as seen from the Sun vantage point. Initially contained in the $X_{swi} -$
 346 Y_{swi} plane upstream of the bow shock, the field lines bend in the Z_{swi} direction to wrap
 347 the magnetopause. The rightmost panels offer a complementary 3D view of the field lines
 348 close to the magnetopause. The great similarity between the modeled draping and the
 349 observed one hides that the former is only constrained by the boundary conditions at
 350 the shock and magnetopause boundaries while the latter also is constrained by the struc-
 351 ture of the magnetosheath flow. When considered, these different constraints explain the
 352 subtle differences seen in this large IMF cone angle limit between lower and upper pan-
 353 els of Fig 3 such as the more pronounced equatorward convergence of field lines in the
 354 model, and are at the root of a much more pronounced disagreement between the two
 355 draping patterns at lower cone angles, as will be explained in the following.

356 In the model (resp. the data), field lines must meet the imposed IMF orientation
 357 at the bow shock and must be exactly (resp. almost) tangential to the magnetopause.
 358 In the magnetostatic case where no electrical current flows within the magnetosheath
 359 volume, the magnetic field lines wrap the magnetopause like paper wraps a candy and
 360 diverge from two singular points at the magnetopause along the normal to the shock where
 361 it is parallel to the IMF. Without any other constraint, field lines just diverge away from
 362 these two singularities as prescribed by the magnetic potential function. This behavior
 363 explains the convergence of the field lines easily seen on the two flanks if looked at from
 364 the Sun standpoint in panel b of Fig. 3. In a perfect 90° IMF cone angle condition, the
 365 two singularities would be perfectly symmetric with respect to $Y_{swi} = 0$. Here, how-
 366 ever, the singularity in the quasi-parallel region is closer to the subsolar region due to
 367 the slight radial component, resulting in slightly more pronounced apparent convergence
 368 of the field lines in the quasi-parallel region of Fig 3b.

369 In contrast, field lines in reality must also comply with the frozen-in condition, im-
 370 posing that magnetically connected solar wind fluid elements must remain so during the
 371 draping. The temporal aspect of the draping then becomes important, and in the large
 372 IMF cone angle limit, follows the schematics of Figure 4a. Among the represented con-
 373 nected points, the red one is the first to meet the shock surface. In the subsolar region,
 374 that element will be strongly decelerated while other connected points remain in motion
 375 at the solar wind speed. Because the IMF cone angle is large, connected fluid elements
 376 are not far apart from one another along the Sun-Earth axis. The element arrived at the
 377 shock in the subsolar region (red dot) is thus still lagging in the slow stagnation flow re-
 378 gion when other connected elements make contact with the shock. Together with the curved
 379 shape of the magnetopause and shock, this gives the observed bow shape to the field line,
 380 reminiscent of the one obtained in the magnetostatic model. Field lines close to the mag-
 381 netopause are deflected around it and thus also bend in the Z directions like in the model,
 382 as seen from the Sun vantage point in Fig 3e. Coincidentally, field lines appear to con-
 383 verge more on the quasi-parallel side than in the quasi-perpendicular side as in the mod-
 384 eled draping. However, the reason here has nothing to do with topological singularities
 385 but is again found in the temporal sequence of the draping. Parts of the field lines that
 386 crossed the shock in the quasi-perpendicular region did so earlier than those in the quasi-
 387 parallel side. Consequently, they had more time to rise away from the $Z_{swi} = 0$ plane
 388 and are thus found slightly more spread apart than their counterparts in the quasi-parallel
 389 side, but in a way that is slightly different than for the modeled field.

390 **3.2 Intermediate IMF cone angle draping**

391 Differences between the model and data become more drastic as the IMF cone an-
 392 gle decreases. As it does so, the parallel shock region moves closer to the subsolar re-
 393 gion. The previously discussed magnetic singularity of the model is now found closer to
 394 the subsolar region as well, as seen in Figure 5a. Clearly, this singularity is not seen in
 395 the data of panel d. In contrast, all the field lines obtained from in-situ data, no mat-
 396 ter how far from subsolar region on the quasi-parallel side, eventually connect to more
 397 sunward regions, as Fig 5d reveals. Consequently, B_x takes negative values all along the
 398 magnetopause on the quasi-parallel side, exactly as it did for large IMF cone angles, and
 399 thus opposed to what the model predicts. This important difference with the magneto-
 400 static model again results from the magnetic field to be frozen in the magnetosheath flow.
 401 Therefore the magnetostatic model, which assume a draping in vacuum, cannot account
 402 for this effect unlike MHD models (Alksne, 1967; Romanelli et al., 2014). This reversal
 403 of the B_x component has been also observed in studies of the Venusian (Rong et al., 2016;
 404 Delva et al., 2017) and Martian (C. Zhang et al., 2022) environments.

405 As before, the part of the field line entered in the subsolar region does not have the
 406 time to re-accelerate before other parts arrive at the shock in the quasi-parallel region.
 407 Field lines entering the quasi-parallel region must thus again connect to the subsolar re-

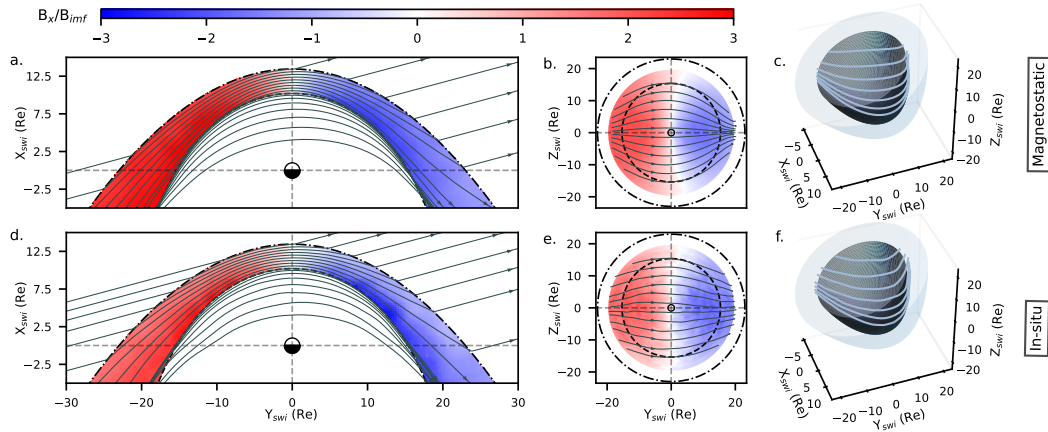


Figure 3. Large IMF cone angle draping. Subset $70^\circ \leq |\theta_{co}| \leq 80^\circ$. Panels a-c to and d-f correspond respectively to magnetostatic (Kobel & Fluckiger, 1994) and in-situ magnetic field. The color maps correspond to B_x/B_{imf} . The grey arrowed lines correspond to the magnetic field lines integrated in 3D (see section 2.8). Panels a and d correspond to the data close to the $Z_{swi} = 0$ plane. Panels b and e correspond to the data close to the magnetopause (Shue et al., 1998). The three-dimension views c and f show the magnetic field lines close to the magnetopause.

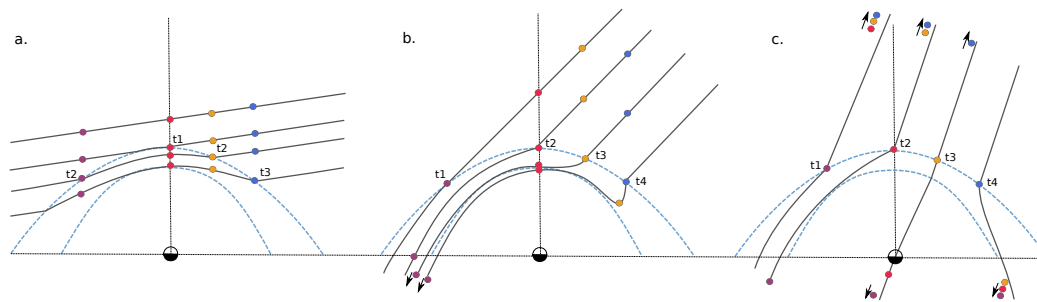


Figure 4. Schematics of the draping mechanism. Panels a, b and c represent the expected draping pattern for the large, intermediate and low IMF cone angle regimes, respectively. t_1 to t_4 represent the arrival time at the bow shock of the different fluid elements (purple, red, orange and blue points) connected by the same magnetic field line.

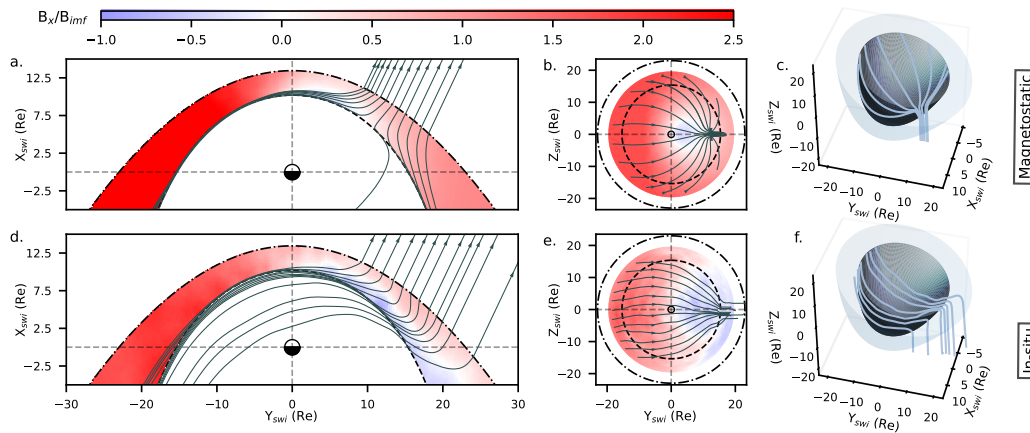


Figure 5. Intermediate IMF cone angle draping. Subset $20^\circ \leq |\theta_{co}| \leq 30^\circ$. The legend is the same as Fig 3.

gion. It is interesting to note, however, that the field lines do not immediately turn towards the dayside as soon as they cross the shock as they do for the large IMF cone angle regime. The key is that for lower IMF cone angle, connected elements are now further apart along X_{swi} in the solar wind, as can be seen on Fig. 4b. They are close enough for the subsolar part of the line to still lag behind by the time they arrive at the shock. However they are too far apart for elements entering the magnetosheath at any point of the quasi-parallel region to pass ahead of connected elements previously entered, as in the large cone angle regime. Upon crossing the bow shock in the quasi-parallel region, field lines thus must continue nightward over some distance before turning back towards the dayside. The sign of B_x is thus necessarily reversed across the magnetosheath in the quasi-parallel side, and an associated steady current sheet exists in the central magnetosheath over a significant portion of the dayside. This electrical current in the magnetosheath volume is the consequence of the transport of the magnetic field in the plasma flow.

As previously noticed in the regime of large IMF cone angles (Fig 3b,e), an asymmetry is visible in the orientation of field lines between the quasi-parallel/perpendicular sides of the magnetosheath as viewed from the Sun (Fig 5b,e). However, here the asymmetry is much more pronounced(Fig 5b). In the modeled draping, this strong asymmetry simply relates to the singularity being now located closer to the subsolar region, towards which field lines must converge. In reality, the asymmetry still relates to the temporal aspect of the draping. For these lower IMF cone angles, connected fluid elements are more separated along X_{swi} . The delay between their arrival at the shock in the quasi-parallel and quasi-perpendicular is thus significantly longer. As a result, field lines in the quasi-perpendicular region have a much longer time to leave the plane $Z = 0$, but they need to remain connected to parts arrived near $Z_{swi} = 0$, leading to the observed asymmetry. The 3D plots on the rightmost panels offer a clear complementary overview of the fundamental difference between the two draping patterns.

3.3 Low IMF cone angle draping

An important question at this point is to what extent the model and data keep exhibiting these distinct patterns as the IMF cone angle decreases even further down to zero. For symmetry reasons, it is clear that for an exactly radial IMF, field lines must spread equally around from the subsolar point. In both the model and data $\theta_{co} = 0$ must thus lead to a null point in that region, as it does only for the model for other IMF ori-

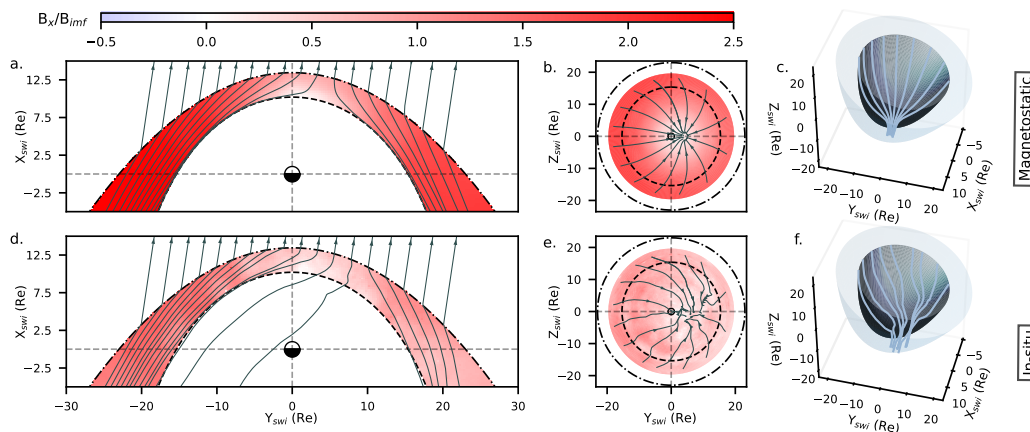


Figure 6. Small IMF cone angle draping. Subset $0^\circ \leq |\theta_{co}| \leq 12.5^\circ$. The legend is the same as Fig 3.

441 entations on the quasi-parallel side. It is unclear at this point, however, whether data
 442 only shows this divergent pattern for the null cone angle or not.

443 The answer is clearly seen on Fig 6, which represents both modeled and observed
 444 draping for a very small but non-zero IMF cone angle. In that regime, it is unsurpris-
 445 ing to see that the modeled draping only differs from previous ones by the position of
 446 the magnetic singularity, now much closer to the subsolar point. It is, however, inter-
 447 esting to notice that the observed draping now also exhibits a similar structure, with an
 448 apparent divergence of the field lines originating approximately from the same location
 449 as in the model.

450 The pattern obtained with data within this low IMF cone angle regime is very noisy,
 451 due to the limited amount of data (Fig 1g) and the likely presence of enhanced fluctu-
 452 ations in that region downstream of the foreshock. However, the results appear again
 453 consistent with the dominant effect of the magnetosheath flow in which the magnetic field
 454 is frozen, and in particular with the temporal aspect of the draping, represented in the
 455 rightmost panel of Fig. 4. For such a low yet non-zero IMF cone angle, connected fluid
 456 elements are now so far from each other along X_{swi} that their arrival time at the shock
 457 is significantly longer than the time it takes for the red element to leave the flow stag-
 458 nation region. The part of the field line entering the subsolar region thus no longer acts
 459 as a bottleneck as it did for the two preceding regimes. Fluid elements arriving at the
 460 shock in the quasi-parallel region are now connected to elements that have traveled a long
 461 distance in the magnetosheath and are located much more nightward. As a result, the
 462 draping pattern is again close to the one obtained in the model, since like in the large
 463 cone angle regime, the magnetosheath flow does not lead to the existence of a current
 464 sheet in the magnetosheath volume, which the model ignores.

465 Although the model and data representations broadly agree again in this very low
 466 IMF cone angle regime, some subtle differences still reveal that the magnetic field is frozen
 467 in the flow in reality while the modeled field ignores this constraint. The field lines ob-
 468 tained from in-situ data (Fig 6d) in the quasi-parallel region indeed appear to come back
 469 towards the magnetopause, consistently with the idea that they should, for some time
 470 at least, still remain connected to their previously entered counterpart in the quasi-perpendicular
 471 side. In contrast, the magnetostatic field lines (Fig 6a), ignoring the frozen-in constraint,
 472 have a completely uncorrelated behavior on both side of the singularity.

473

3.4 Role of the magnetosheath flow in structuring the draping

474

475

476

477

478

479

480

481

482

483

484

485

486

487

488

489

490

491

492

493

494

495

496

497

498

499

500

501

502

503

504

Previous figures gave us a qualitative and consistent picture of the importance of the frozen-in behavior for understanding the structure of the field line draping around the magnetopause. The following analysis now tests this interpretation in a more quantitative way. We focus on Fig. 7, where each panel represents the dayside magnetosphere in the $X_{swi}-Y_{swi}$ plane for each of the three draping regimes previously identified. Each panel shows green and red magnetic field lines, obtained from the magnetostatic model and in-situ data, respectively. Ion flow stream lines, obtained from in-situ data in a similar way as for the magnetic field, are also represented. Each line is again the result of a three-dimensional integration. The red and green magnetic field lines are chosen to intersect the bow shock at an arbitrary but identical position, located in the quasi-parallel side of the system. Knowing the point at which the magnetic field line intersects the bow shock, the IMF cone angle, and given a solar wind velocity assumed steady, it is easy to compute the time delay between the time of the representation and that at which the field line crossed the bow shock at any other point corresponding to the time during which it has propagated into the magnetosheath (see annex for the details concerning the determination of the time delay). Multiple points are thus chosen on the bow shock as starting points of flow lines. 3D flow lines, integrated during the time delay associated to their starting point, stop right on top of the magnetic field line obtained from data for the large and intermediate IMF cone angle regimes (Fig 7a,b), as expected from the frozen-in condition. The agreement is remarkable, considering that the integration time only assumes a constant solar wind velocity, a steady IMF orientation, and, above all, knowing that the magnetic field and velocity are two independent in-situ measurements. The flow line integration also agrees better with the magnetic field data than with that of the model in the large cone angle one, despite their very close behavior. This analysis clearly confirms previous qualitative interpretations in each of the IMF cone angle regimes. In the very IMF low cone angle limit (Fig 7c), the results remain consistent, even if the scarcity of the data increases a lot the uncertainty associated with the field line integration. In addition the large delay between arrival times at the shock, of the different part of the magnetic field line, leaves room for many processes to invalidate the steady state assumption our study is based on. Furthermore, it is not clear to what extent fluid elements arriving at the shock remain connected to nightside regions for such long times.

505

4 conclusion

506

507

508

509

510

511

512

513

514

515

516

517

518

519

520

521

522

523

524

It has been known for decades that the interplanetary magnetic field drapes around the magnetosphere of the Earth as it crosses the bow shock. Only global magnetohydrodynamics numerical models have provided a complete, global and three-dimensional structure of the draping for a given IMF orientation. Through the use of innovative machine learning based in-situ detection, this study offers such a global view from a purely observational standpoint. To emphasize the role of the magnetosheath flow, the observed draping is compared to that predicted by the magnetostatic model of Kobel et al. 1994, where the plasma is missing. For large ($|\theta_{co}| > 45^\circ \pm 5^\circ$) or extremely small ($12.5^\circ \pm 2.5^\circ < |\theta_{co}|$) IMF cone angles, the global draping is found to be qualitatively consistent with a magnetostatic draping assuming no current in the magnetosheath volume (Kobel & Fluckiger, 1994). In contrast, data clearly and fundamentally disagree with the magnetostatic draping in the intermediate cone angle regime ($12.5^\circ \pm 2.5^\circ < |\theta_{co}| < 45.0^\circ \pm 5^\circ$) and angular deviations can be as high as about 180° in some portions of the quasi-parallel magnetosheath. In the data, field lines fold onto the magnetopause surface and are constrained to remain frozen in solar wind fluid elements. This folding is associated to a large scale current sheet at mid-depth in the quasi-parallel magnetosheath. This scenario is further quantitatively validated by mapping magnetic field lines with the 3D integration of the independently measured flow velocity. The detailed structure of the magnetic field draping, shown in our study to be intrinsically linked to the radial

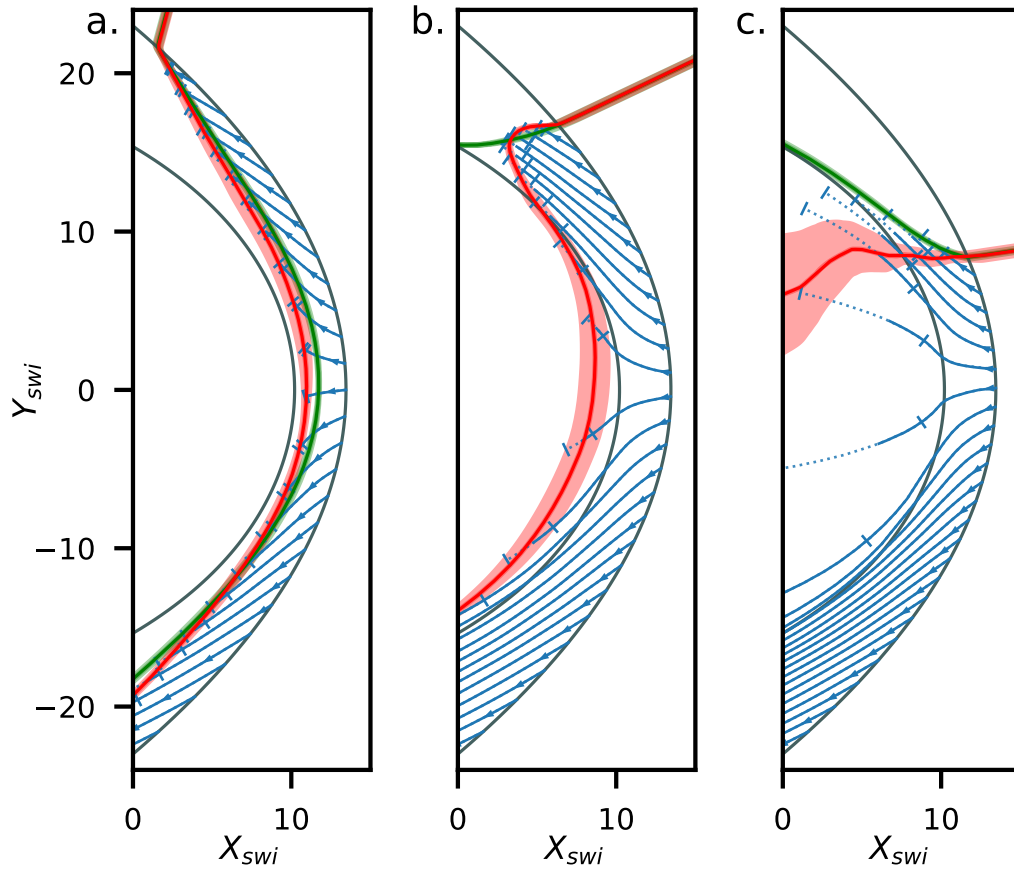


Figure 7. Quantitative estimate of the flux freezing condition. Panels a, b and c are associated with the large, intermediate and low IMF cone angle regimes, respectively. The red and green lines represent the magnetic field lines obtained from in-situ data and the magnetostatic model (Kobel & Fluckiger, 1994), respectively. The uncertainty on the position of the field lines is represented with the shaded area and is calculated with the integration of 1500 field lines with starting points in a sphere of $0.5 R_e$ of diameter. The solid blue lines correspond to the plasma streamlines integrated in 3D with in-situ measurements of the velocity (see method). The error bars are determined for each line by calculating the integration times (see method) corresponding to the first and third quartile of the distribution of the IMF cone angle in each subset.

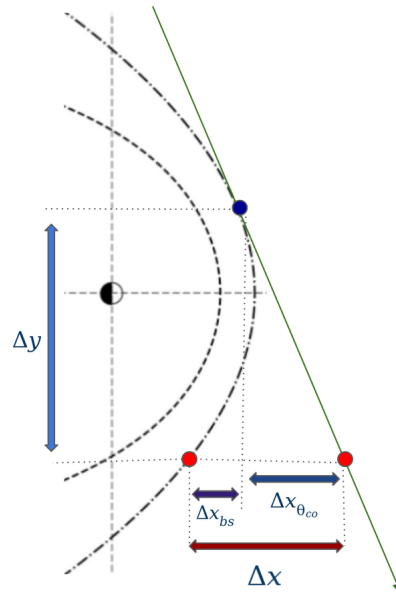


Figure 8. Determination of the integration time of the flow lines. The streamline is integrated from the blue point. This point is magnetically connected to the red point. The streamline is integrated during the time taken for the red point to reach the bow shock, estimated via Eq. 2 . $\Delta X_{co} = \Delta Y / \tan \theta_{co}$ is the distance produced by the inclination of the IMF in respect of the X axis and ΔX_{bs} is the additional distance produced by the shock's shape.

525 flow of the magnetosheath plasma, constitutes the immediate boundary condition for the
 526 magnetosphere system. It is in particular relevant to where magnetic reconnection oc-
 527 curs and operate, and thus how the Earth system couples to its environment. Our study
 528 also shows how having decades of data from multiple missions enables the assessment
 529 of global yet detailed and quantitative properties of the Earth magnetosphere despite
 530 the fundamentally local character of in-situ measurements. Although considerably less
 531 data exists, these results are also relevant to the case of other planets and obstacles to
 532 magnetized plasma flows.

533 **5 Annex : Time integration of plasma flow lines**

534 The time delay Δt used to integrate flow lines in section 2.8 can be estimated by
 535 eq. 2, where

$$\Delta t = \frac{\frac{\Delta Y}{\tan \theta_{co}} + \Delta X_{bs}}{V_{sw}} \quad (2)$$

536 ΔY is the distance along the Y axis between the start points at the bow shock of
 537 the magnetic field and flow lines corresponding to the red and blue points in Fig. 8, re-
 538 spectively. ΔX_{bs} is the distance along the X axis between those start points produced
 539 by the bow shock shape, as shown in Fig. 8 . θ_{co} corresponds to the median value of the
 540 subset's IMF cone angle range. The solar wind velocity V_{sw} is equal to 1 because each
 541 magnetosheath velocity measurement is normalized by its causal solar wind speed. The
 542 uncertainties of the flow lines are dominated by the dependence of Eq. 2 to the IMF cone
 543 angle range. Therefore the first and third quartiles of this angle range are used to cal-

544 culate the longest and shortest integration times, respectively, and used to represent the
 545 uncertainty for the tip of the flow line.

546 Data Availability Statement

547 The in-situ data are available by using the Speasy package ([https://github.com/](https://github.com/SciQLop/speasy)
 548 [SciQLop/speasy](https://github.com/SciQLop/speasy)). It allows to access the data on the CDAweb database ([https://cdaweb](https://cdaweb.gsfc.nasa.gov)
 549 [.gsfc.nasa.gov](https://cdaweb.gsfc.nasa.gov)) for the THEMIS mission, and AMDA database ([http://amda.irap](http://amda.irap.omp.eu)
 550 [.omp.eu](http://amda.irap.omp.eu)) for Cluster, DoubleStar, and MMS missions.

551 References

- 552 Alksne, A. Y. (1967, February). The steady-state magnetic field in the transition re-
 553 gion between the magnetosphere and the bow shock. , *15*(2), 239-245. doi: 10
 554 .1016/0032-0633(67)90192-4
- 555 Auster, H. U., Glassmeier, K. H., Magnes, W., Aydogar, O., Baumjohann, W.,
 556 Constantinescu, D., ... Wiedemann, M. (2008, Dec). The THEMIS Flux-
 557 gate Magnetometer. *Scientific Studies of Reading*, *141*(1-4), 235-264. doi:
 558 10.1007/s11214-008-9365-9
- 559 Balogh, A., Carr, C., Acuña, M., Dunlop, M., Beek, T., Brown, P., ... Schwingen-
 560 schuh, K. (2001, 10). The cluster magnetic field investigation: Overview
 561 of in-flight performance and initial results. *Annales Geophysicae*, *19*. doi:
 562 10.5194/angeo-19-1207-2001
- 563 Behannon, K. W., & Fairfield, D. H. (1969). Spatial variations of the magnetosheath
 564 magnetic field. *Planetary and Space Science*, *17*(10), 1803–1816. doi: 10.1016/
 565 0032-0633(69)90056-7
- 566 Bertucci, C., Duru, F., Edberg, N., Fraenz, M., Martinecz, C., Szego, K., & Vais-
 567 berg, O. (2011). The Induced Magnetospheres of Mars, Venus, and Titan.
 568 *Space Science Reviews*, *162*(1-4), 113–171. doi: 10.1007/s11214-011-9845-1
- 569 Breuillard, H., Dupuis, R., Retino, A., Le Contel, O., Amaya, J., & Lapenta, G.
 570 (2020, September). Automatic classification of plasma regions in near-Earth
 571 space with supervised machine learning: application to Magnetospheric Multi
 572 Scale 2016-2019 observation. *Frontiers in Astronomy and Space Sciences*, *7*,
 573 55. doi: 10.3389/fspas.2020.00055
- 574 Carr, C., Brown, P., Zhang, T. L., Gloag, J., Horbury, T., Lucek, E., ... Richter,
 575 I. (2005, Nov). The Double Star magnetic field investigation: instrument
 576 design, performance and highlights of the first year's observations. *Annales*
 577 *Geophysicae*, *23*(8), 2713-2732. doi: 10.5194/angeo-23-2713-2005
- 578 Cassak, P. A., & Fuselier, S. A. (2016, January). Reconnection at Earth's Day-
 579 side Magnetopause. In W. Gonzalez & E. Parker (Eds.), *Magnetic re-*
 580 *connection: Concepts and applications* (Vol. 427, p. 213). doi: 10.1007/
 581 978-3-319-26432-5_6
- 582 Coleman, I. J. (2005, 03). A multi-spacecraft survey of magnetic field line draping
 583 in the dayside magnetosheath. *Annales Geophysicae*, *23*(3), 885 – 900. doi: 10
 584 .5194/angeo-23-885-2005
- 585 Crooker, N. U., Luhmann, J. G., Russell, C., Smith, E. J., Spreiter, J. R., & Sta-
 586 hara, S. S. (1985, 04). Magnetic field draping against the dayside magne-
 587 topause. *Journal of Geophysical Research (Space Physics)*, *90*(A4), 3505 –
 588 3510. doi: 10.1029/ja090ia04p03505
- 589 Delva, M., Volwerk, M., Jarvinen, R., & Bertucci, C. (2017). Asymmetries in the
 590 Magnetosheath Field Draping on Venus' Nightside. *Journal of Geophysical Re-*
 591 *search: Space Physics*, *122*(10), 10,396–10,407. doi: 10.1002/2017ja024604
- 592 Dimmock, A. P., Hietala, H., & Zou, Y. (2020, June). Compiling Magnetosheath
 593 Statistical Data Sets Under Specific Solar Wind Conditions: Lessons Learnt

- 594 From the Dayside Kinetic Southward IMF GEM Challenge. *Earth and Space*
 595 *Science*, 7, 01095. doi: 10.1029/2020EA001095
- 596 Dimmock, A. P., & Nykyri, K. (2013, August). The statistical mapping of mag-
 597 netosheath plasma properties based on THEMIS measurements in the mag-
 598 netosheath interplanetary medium reference frame. *Journal of Geophysical*
 599 *Research (Space Physics)*, 118(8), 4963-4976. doi: 10.1002/jgra.50465
- 600 Fairfield, D. H. (1967). *The ordered magnetic field of the magnetosheath* (Vol. 72).
 601 doi: 10.1029/jz072i023p05865
- 602 Génot, V., Broussillou, L., Budnik, E., Hellinger, P., Trávníček, P. M., Lucek, E., &
 603 Dandouras, I. (2011, 10). Timing mirror structures observed by Cluster with
 604 a magnetosheath flow model. *Annales Geophysicae*, 29(1), 1849 – 1860. doi:
 605 10.5194/angeo-29-1849-2011
- 606 Jelinek, K., Nemeček, Z., & Safrankova, J. (2012, April). Spatial profiles of mag-
 607 netosheath plasma and magnetic field parameters and their variations. In *Egu*
 608 *general assembly conference abstracts* (p. 9175).
- 609 Jelínek, K., Němeček, Z., & Šafránková, J. (2012, May). A new approach to mag-
 610 netopause and bow shock modeling based on automated region identification.
 611 *Journal of Geophysical Research (Space Physics)*, 117(A5), A05208. doi:
 612 10.1029/2011JA017252
- 613 Jones, G. H., Rees, A., Balogh, A., & Forsyth, R. J. (2002). The draping of helio-
 614 spheric magnetic fields upstream of coronal mass ejecta. *Geophysical Research*
 615 *Letters*, 29(11), 15-1-15-4. doi: 10.1029/2001gl014110
- 616 Juhász, A., & Horányi, M. (1997). Dynamics of charged space debris in the
 617 Earth's plasma environment. *Journal of Geophysical Research: Space Physics*,
 618 102(A4), 7237–7246. doi: 10.1029/96ja03672
- 619 Juhász, A., & Horányi, M. (1999). Magnetospheric screening of cosmic dust. *Journal*
 620 *of Geophysical Research: Space Physics*, 104(A6), 12577–12583. doi: 10.1029/
 621 1999ja900091
- 622 Kallio, E. J., & Koskinen, H. E. J. (2000, December). A semiempirical magne-
 623 tosheath model to analyze the solar wind-magnetosphere interaction. *JGR*,
 624 105(A12), 27469-27480. doi: 10.1029/2000JA900086
- 625 Kaymaz, Z. (1998, 04). IMP 8 magnetosheath field comparisons with models. *An-*
 626 *nales Geophysicae*, 16(4), 376 – 387. doi: 10.1007/s00585-998-0376-3
- 627 Kaymaz, Z., Luhmann, J. G., Fedder, J. A., Lyon, J. G., Spreiter, J. R., & Stahara,
 628 S. S. (1996, 06). Evidence for reverse draping of magnetosheath field around
 629 the magnetosphere in IMP 8 observations for northward interplanetary mag-
 630 netic field. *Journal of Geophysical Research (Space Physics)*, 101(A6), 13321 –
 631 13326. doi: 10.1029/96ja00509
- 632 Kaymaz, Z., & Siscoe, G. (2006). Field-Line Draping Around ICMES. *Solar Physics*,
 633 239(1-2), 437–448. doi: 10.1007/s11207-006-0308-x
- 634 Kaymaz, Z., Siscoe, G., & Luhmann, J. G. (1992). IMF draping around the Geo-
 635 tail: IMP 8 observations. *Geophysical Research Letters*, 19(8), 829–832. doi:
 636 10.1029/92gl00403
- 637 King, J. H., & Papitashvili, N. E. (2005, February). Solar wind spatial scales in and
 638 comparisons of hourly Wind and ACE plasma and magnetic field data. *Jour-*
 639 *nal of Geophysical Research (Space Physics)*, 110(A2), A02104. doi: 10.1029/
 640 2004JA010649
- 641 Kobel, E., & Fluckiger, E. O. (1994, December). A model of the steady state mag-
 642 netic field in the magnetosheath. *JGR*, 99(A12), 23617-23622. doi: 10.1029/
 643 94JA01778
- 644 Koenders, C., Goetz, C., Richter, I., Motschmann, U., & Glassmeier, K.-H. (2016).
 645 Magnetic field pile-up and draping at intermediately active comets: re-
 646 sults from comet 67P/Churyumov–Gerasimenko at 2.0 AU. *Monthly No-*
 647 *tices of the Royal Astronomical Society*, 462(Suppl.1), S235–S241. doi:
 648 10.1093/mnras/stw2480

- 649 Kramer, O. (2013). K-nearest neighbors. In *Dimensionality reduction with unsuper-*
 650 *vised nearest neighbors* (pp. 13–23). Berlin, Heidelberg: Springer Berlin Heidel-
 651 berg. Retrieved from https://doi.org/10.1007/978-3-642-38652-7_2 doi:
 652 10.1007/978-3-642-38652-7_2
- 653 Longmore, M., Schwartz, S., & Lucek, E. (2006, 03). Rotation of the magnetic field
 654 in Earth’s magnetosheath by bulk magnetosheath plasma flow. *Annales Geo-*
 655 *physicae*, *24*(1), 339 – 354. doi: 10.5194/angeo-24-339-2006
- 656 Masters, A. (2014). Magnetic reconnection at Uranus’ magnetopause. *Jour-*
 657 *nal of Geophysical Research: Space Physics*, *119*(7), 5520–5538. doi: 10.1002/
 658 2014ja020077
- 659 Masters, A. (2015). Magnetic reconnection at Neptune’s magnetopause.
 660 *Journal of Geophysical Research: Space Physics*, *120*(1), 479–493. doi:
 661 10.1002/2014ja020744
- 662 Masters, A. (2017, 11). Model-Based Assessments of Magnetic Reconnection and
 663 Kelvin-Helmholtz Instability at Jupiter’s Magnetopause. *Journal of Geophysi-*
 664 *cal Research (Space Physics)*, *122*(1), 11. doi: 10.1002/2017ja024736
- 665 McComas, D. J., Gosling, J. T., Winterhalter, D., & Smith, E. J. (1988). Inter-
 666 planetary magnetic field draping about fast coronal mass ejecta in the outer
 667 heliosphere. *Journal of Geophysical Research: Space Physics*, *93*(A4), 2519–
 668 2526. doi: 10.1029/ja093ia04p02519
- 669 McComas, D. J., Spence, H. E., Russell, C. T., & Saunders, M. A. (1986, July). The
 670 average magnetic field draping and consistent plasma properties of the venus
 671 magnetotail. , *91*(A7), 7939-7953. doi: 10.1029/JA091iA07p07939
- 672 McFadden, J. P., Carlson, C. W., Larson, D., Ludlam, M., Abiad, R., Elliott, B., ...
 673 Angelopoulos, V. (2008, Dec). The THEMIS ESA Plasma Instrument and
 674 In-flight Calibration. *Scientific Studies of Reading*, *141*(1-4), 277-302. doi:
 675 10.1007/s11214-008-9440-2
- 676 Merka, J., Szabo, A., Narock, T. W., King, J. H., Paularena, K. I., & Richardson,
 677 J. D. (2003, February). A comparison of IMP 8 observed bow shock positions
 678 with model predictions. *Journal of Geophysical Research (Space Physics)*,
 679 *108*(A2), 1077. doi: 10.1029/2002JA009384
- 680 Nguyen, G., Aunai, N., Michotte de Welle, B., Jeandet, A., Lavraud, B., & Fontaine,
 681 D. (2022, January). Massive Multi-Mission Statistical Study and An-
 682 alytical Modeling of the Earth’s Magnetopause: 2. Shape and Location.
 683 *Journal of Geophysical Research (Space Physics)*, *127*(1), e29774. doi:
 684 10.1029/2021JA029774
- 685 Nguyen, G., Aunai, N., Welle, B. M. d., Jeandet, A., Lavraud, B., & Fontaine, D.
 686 (2022). Massive Multi-Mission Statistical Study and Analytical Modeling of
 687 the Earth’s Magnetopause: 1. A Gradient Boosting Based Automatic Detec-
 688 tion of Near-Earth Regions. *Journal of Geophysical Research: Space Physics*,
 689 *127*(1). doi: 10.1029/2021ja029773
- 690 Ohtani, S. K. S., & kokubun. (1991). Magnetic properties of the high-latitude tail
 691 boundary: Draping of magnetosheath field lines and tail-aligned current. *JGR*,
 692 *96*(A6), 1 – 10. doi: 10.1029/91ja00570
- 693 Olshevsky, V., Khotyaintsev, Y. V., Lalti, A., Divin, A., Delzanno, G. L., Anderzén,
 694 S., ... Markidis, S. (2021, October). Automated Classification of Plasma Re-
 695 gions Using 3D Particle Energy Distributions. *Journal of Geophysical Research*
 696 *(Space Physics)*, *126*(10), e29620. doi: 10.1029/2021JA029620
- 697 Opher, M., Stone, E. C., & Gombosi, T. I. (2007). The Orientation of the Local In-
 698 terstellar Magnetic Field. *Science*, *316*(5826), 875–878. doi: 10.1126/science
 699 .1139480
- 700 Pedregosa, F., Varoquaux, G., Gramfort, A., Michel, V., Thirion, B., Grisel, O., ...
 701 Duchesnay, E. (2011). Scikit-learn: Machine learning in Python. *Journal of*
 702 *Machine Learning Research*, *12*, 2825–2830.
- 703 Petrinec, S. M. (2016, July). Draping of strongly flow-aligned interplanetary mag-

- 704 netic field about the magnetopause. *Advances in Space Research*, 58(2), 175-
 705 180. doi: 10.1016/j.asr.2015.10.001
- 706 Pfrommer, C., & Dursi, J. (2010). Detecting the orientation of magnetic fields in
 707 galaxy clusters. *Nature Physics*, 6(7), 520–526. doi: 10.1038/nphys1657
- 708 Pogorelov, N. V., Fraternali, F., Kim, T. K., Burlaga, L. F., & Gurnett, D. A.
 709 (2021). Magnetic Field Draping of the Heliopause and Its Consequences for
 710 Radio Emission in the Very Local Interstellar Medium. *The Astrophysical
 711 Journal Letters*, 917(2), L20. doi: 10.3847/2041-8213/ac14bd
- 712 Pollock, C., Moore, T., Jacques, A., Burch, J., Gliese, U., Saito, Y., ... Zeuch, M.
 713 (2016, Mar). Fast Plasma Investigation for Magnetospheric Multiscale. *Scien-
 714 tific Studies of Reading*, 199(1-4), 331-406. doi: 10.1007/s11214-016-0245-4
- 715 Reidler, W., Schwingenschuh, K., Yeroshenko, Y. G., Styashkin, V. A., & Russell,
 716 C. T. (1986). Magnetic field observations in comet Halley's coma. *Nature*,
 717 321(Suppl 6067), 288–289. doi: 10.1038/321288a0
- 718 Rème, H., Aoustin, C., Bosqued, J. M., Dandouras, I., Lavraud, B., Sauvaud,
 719 J. A., ... Sonnerup, B. (2001, Oct). First multispacecraft ion measure-
 720 ments in and near the Earth's magnetosphere with the identical Cluster ion
 721 spectrometry (CIS) experiment. *Annales Geophysicae*, 19, 1303-1354. doi:
 722 10.5194/angeo-19-1303-2001
- 723 Rème, H., Dandouras, I., Aoustin, C., Bosqued, J. M., Sauvaud, J. A., Vallat, C.,
 724 ... Lundin, R. (2005, November). The HIA instrument on board the Tan
 725 Ce 1 Double Star near-equatorial spacecraft and its first results. *Annales
 726 Geophysicae*, 23(8), 2757-2774.
- 727 Romanelli, N., Gómez, D., Bertucci, C., & Delva, M. (2014, July). Steady-state
 728 Magnetohydrodynamic Flow around an Unmagnetized Conducting Sphere. ,
 729 789(1), 43. doi: 10.1088/0004-637X/789/1/43
- 730 Romashets, E. P., & Vandas, M. (2019, April). Analytic Modeling of Magnetic Field
 731 in the Magnetosheath and Outer Magnetosphere. *Journal of Geophysical Re-
 732 search (Space Physics)*, 124(4), 2697-2710. doi: 10.1029/2018JA026006
- 733 Rong, Z. J., Barabash, S., Futaana, Y., Stenberg, G., Zhang, T. L., Wan, W. X., ...
 734 Zhong, J. (2014, November). Morphology of magnetic field in near-Venus mag-
 735 netotail: Venus express observations. *Journal of Geophysical Research (Space
 736 Physics)*, 119(11), 8838-8847. doi: 10.1002/2014JA020461
- 737 Rong, Z. J., Stenberg, G., Wei, Y., Chai, L. H., Futaana, Y., Barabash, S., ...
 738 Shen, C. (2016, November). Is the flow-aligned component of IMF really
 739 able to impact the magnetic field structure of Venusian magnetotail? *Jour-
 740 nal of Geophysical Research (Space Physics)*, 121(11), 10,978-10,993. doi:
 741 10.1002/2016JA022413
- 742 Russell, C. T., Anderson, B. J., Baumjohann, W., Bromund, K. R., Dearborn,
 743 D., Fischer, D., ... Richter, I. (2016, Mar). The Magnetospheric Multi-
 744 scale Magnetometers. *Scientific Studies of Reading*, 199(1-4), 189-256. doi:
 745 10.1007/s11214-014-0057-3
- 746 Safránková, J., Nemecek, Z., Dusík, S., Prech, L., Sibeck, D. G., & Borodkova, N. N.
 747 (2002, March). The magnetopause shape and location: a comparison of the
 748 Interball and Geotail observations with models. *Annales Geophysicae*, 20(3),
 749 301-309. doi: 10.5194/angeo-20-301-2002
- 750 Schmid, D., Narita, Y., Plaschke, F., Volwerk, M., Nakamura, R., & Baumjohann,
 751 W. (2021a). Magnetosheath plasma flow model around Mercury. *Annales
 752 Geophysicae*, 39(3), 563–570. doi: 10.5194/angeo-39-563-2021
- 753 Schmid, D., Narita, Y., Plaschke, F., Volwerk, M., Nakamura, R., & Baumjohann,
 754 W. (2021b). Pick-Up Ion Cyclotron Waves Around Mercury. *Geophysical
 755 Research Letters*, 48(9). doi: 10.1029/2021gl092606
- 756 Shue, J. H., Song, P., Russell, C. T., Steinberg, J. T., Chao, J. K., Zastenker, G., ...
 757 Kawano, H. (1998, August). Magnetopause location under extreme solar wind
 758 conditions. *JGR*, 103(A8), 17691-17700. doi: 10.1029/98JA01103

- 759 Spreiter, J. R., Summers, A. L., & Alksne, A. Y. (1966). Hydromagnetic flow around
 760 the magnetosphere. *Planetary and Space Science*, *14*(3), 223–253. doi: 10
 761 .1016/0032-0633(66)90124-3
- 762 Sulaiman, A. H., Masters, A., Dougherty, M. K., & Jia, X. (2014, 07). The magnetic
 763 structure of Saturn’s magnetosheath. *Journal of Geophysical Research (Space
 764 Physics)*, *119*(7), 5651 – 5661. doi: 10.1002/2014ja020019
- 765 Trattner, K. J., Petrinec, S. M., & Fuselier, S. (2021, 04). The Location of Magnetic
 766 Reconnection at Earth’s Magnetopause. *Space Science Reviews*, *217*(3), 1 – 47.
 767 doi: 10.1007/s11214-021-00817-8
- 768 Turc, L., Fontaine, D., Savoini, P., & Kilpua, E. K. J. (2014, February). A model of
 769 the magnetosheath magnetic field during magnetic clouds. *Annales Geophysi-
 770 cae*, *32*(2), 157-173. doi: 10.5194/angeo-32-157-2014
- 771 Vandas, M., Nemecek, Z., Safrankova, J., Romashets, E. P., & Hajoš, M. (2020, 03).
 772 Comparison of Observed and Modeled Magnetic Fields in the Earth’s Magne-
 773 tosheath. *Journal of Geophysical Research (Space Physics)*, *125*(3), e27705.
 774 doi: 10.1029/2019ja027705
- 775 Vandas, M., & Romashets, E. P. (2019, 11). Modeling of magnetic field in the
 776 magnetosheath using elliptic coordinates. *Planetary and Space Science*, *178*,
 777 104692. doi: 10.1016/j.pss.2019.07.007
- 778 Wang, Y., Sibeck, D. G., Merka, J., Boardsen, S. A., Karimabadi, H., Sipes, T. B.,
 779 ... Lin, R. (2013, May). A new three-dimensional magnetopause model with
 780 a support vector regression machine and a large database of multiple space-
 781 craft observations. *Journal of Geophysical Research (Space Physics)*, *118*(5),
 782 2173-2184. doi: 10.1002/jgra.50226
- 783 Zhang, C., Rong, Z., Klinger, L., Nilsson, H., Shi, Z., He, F., ... Wei, Y. (2022, Au-
 784 gust). Three-Dimensional Configuration of Induced Magnetic Fields Around
 785 Mars. *Journal of Geophysical Research (Planets)*, *127*(8), e07334. doi: 10
 786 .1029/2022JE007334
- 787 Zhang, H., Fu, S., Pu, Z., Lu, J., Zhong, J., Zhu, C., ... Liu, L. (2019, August).
 788 Statistics on the Magnetosheath Properties Related to Magnetopause Magnetic
 789 Reconnection. *APJ*, *880*(2), 122. doi: 10.3847/1538-4357/ab290e